

# Supplemental Material for “Hierarchical structure of the energy landscape in the Voronoi model of dense tissue”

Diogo E. P. Pinto<sup>1,2</sup>, Daniel M. Sussman<sup>3</sup>, Margarida M. Telo da Gama<sup>1,2</sup> and Nuno A. M. Araújo<sup>1,2</sup>

<sup>1</sup> Centro de Física Teórica e Computacional, Faculdade de Ciências,  
Universidade de Lisboa, 1749-016 Lisboa, Portugal.

<sup>2</sup> Departamento de Física, Faculdade de Ciências,  
Universidade de Lisboa, 1749-016 Lisboa, Portugal.

<sup>3</sup> Department of Physics, Emory University, Atlanta, GA, USA

## A. Contact metric

If we use the same perturbation as in the energy metric ( $\varepsilon_{max} = 0.1\sqrt{N}$ ) we are only able to reach distances of  $d^X(a, b) \approx 0.23$ . By making the same analysis as in the main text, we find the results plotted in Fig. S1. From these matrices it is possible to see the structure of the basins more clearly but the results remain qualitatively the same and the system does not appear to be ultrametric.

## B. $k_A \neq 1$ cases

Here we explore the changes to the energy landscape for different  $k_A$ . We explore the values  $k_A = \{0, 10^{-2}, 10^0, 10^2\}$ . For finite  $k_A$  a transition to the fluid-like state never occurs and the system is always rigid. Nonetheless, features of a transition between rigid states are still present for all  $k_A$ .

In Fig. S2 we can observe how the different  $k_A$  change the hierarchy of the energy landscape, using the generalized distance to ultrametricity (Eq. (4)). We find that the results are similar for the different  $k_A$ , especially  $k_A = 1$  and  $k_A = 100$ . For  $k_A = 0.01$ , the variance of  $D_N^E$  increases significantly around  $p_0 = 3.81$ , while for the other systems this is not as pronounced. This is due to the fact that the energy landscape partially flattens and there is coexistence between basins with multiple sub-basins and basins which are almost flat where any (small) perturbation always leads to the same minimum.

Although the variance seems to reduce significantly for  $p_0 = 3.83$ , this might be due to the presence of multi-fold vertices. Since we are not able to take these vertices into account in our simulations, we have to discard them. This leaves a smaller pool of minima to sample which might lead to smaller fluctuations. The qualitative properties of the different phases described in the main text can be seen in the matrices shown in Fig. S2.

## C. Energy metric with similar distance distributions

There is a dependence of the distances explored with  $p_0$  when using the energy metric, with increasing  $p_0$  leading to larger distances. Here, we change  $\varepsilon_{max}$  for different  $p_0$ ,

in such a way that similar ranges of normalized energy metric distance are explored. In Fig. S3 we show how the generalized distance to ultrametricity,  $D_N^E$ , changes as a function of  $p_0$ , using a constant  $\varepsilon_{max}$  and a variable one that depends on  $p_0$ . We observe that although the values change slightly, the qualitative description of the results remains the same.

## D. Different perturbation protocols

To analyze the sensitivity to the perturbation protocol, we tested different approaches. Aside from the protocol described in the main text we introduce two new ones, one based on Gaussian perturbations and another where some skeweness is added.

In the Gaussian perturbation (G), we start by creating a perturbation vector  $\vec{P}_\varepsilon = [X_0, X_1, X_2, X_3, \dots, X_{2N-1}]$ , where  $N$  is the number of cells,  $X_{2i} = \mathcal{N}(0, 1)$  is the perturbation to cell  $i$  along the  $x$ -axis and  $X_{2i+1} = \mathcal{N}(0, 1)$  is the one along the  $y$ -axis. Here,  $\mathcal{N}(0, 1)$  represents a normal distribution with mean  $\mu = 0$  and standard deviation  $\sigma = 1$ . Then we subtract the global translation of the system after perturbation. Finally, we multiply the perturbation vector by  $\varepsilon$ , which is a uniformly distributed random variable between 0 and  $\varepsilon_{max}$ . With this formulation, the norm of the perturbation vector will scale as  $|\vec{P}_\varepsilon| = P_\varepsilon = \varepsilon\sqrt{2N}\sigma$ .

In the Skewed perturbation (S), we start by defining a perturbation vector  $\vec{P}_\varepsilon = [X_0, X_1, X_2, X_3, \dots, X_{2N-1}]$ , where  $X_{2i} = \mathcal{N}(0, 1) + \mathcal{E}(0.5)$  is the perturbation to cell  $i$  along the  $x$ -axis and  $X_{2i+1} = \mathcal{N}(0, 1) + \mathcal{E}(0.5)$  is the one along the  $y$ -axis. Here,  $\mathcal{E}(0.5)$  represents a Poisson distribution with rate  $\lambda = 0.5$ . Then we subtract the global translation of the system after perturbation. Finally, we multiply the perturbation vector by  $\varepsilon$ , which is a uniformly distributed random variable between 0 and  $\varepsilon_{max}$ . By adding a Poisson distribution we are skewing the positive Gaussian tail. With this formulation, the norm of the perturbation vector will scale as  $|\vec{P}_\varepsilon| = P_\varepsilon = \varepsilon\sqrt{2N(\sigma^2 + 1/\lambda^2)}$ .

In Fig. S4 is represented the generalized distance to ultrametricity,  $D_N^E$ , as a function of  $p_0$ , calculated using multiple perturbations to the same minimum. The maximum perturbation displacement was fixed at  $\varepsilon_{max} = 0.1\sqrt{N}$  for all protocols. We observe that the different

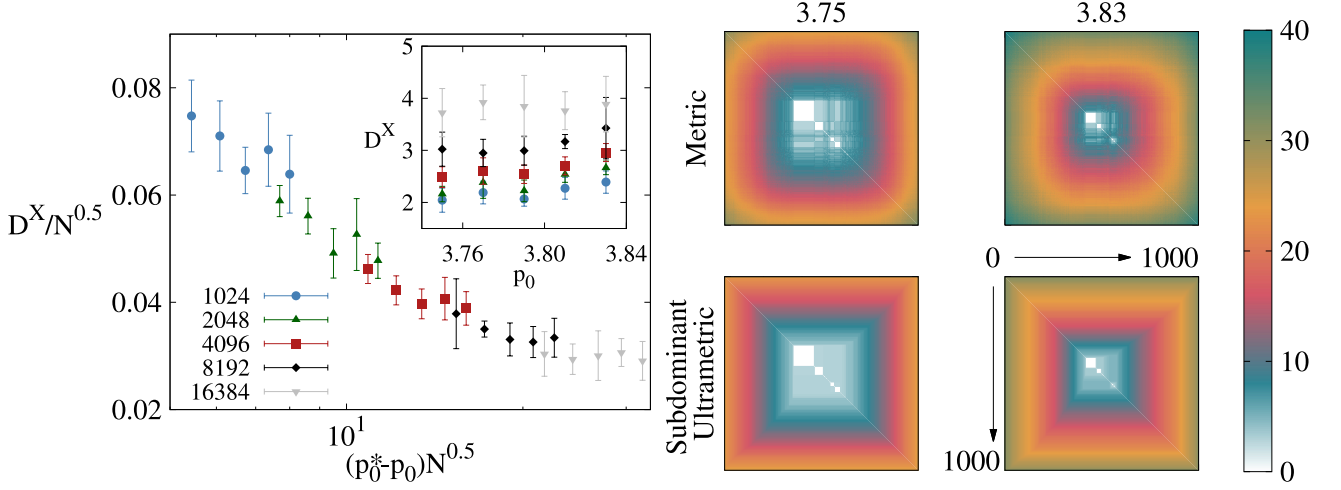


FIG. S1. On the right is a schematic representation of the distances between minima according to the contact metric and its corresponding subdominant ultrametric. We show the matrices for  $p_0 = 3.75, 3.83$ , with 1000 different minima and  $N = 4096$ . The different distances are grouped using a single-linkage clustering algorithm. On the left is a plot of the normalized distance to ultrametricity (Eq. (4)) as a function of  $(p_0^* - p_0)N^{0.5}$ , where we have chosen  $p_0^* = 3.92 \pm 0.01$ , for  $N = 1024, 2048, 4096, 8192, 16384$ . The inset shows the same results without this scaling. All results are averages of 10 initial configurations subject to 100 perturbations and minimizations each.

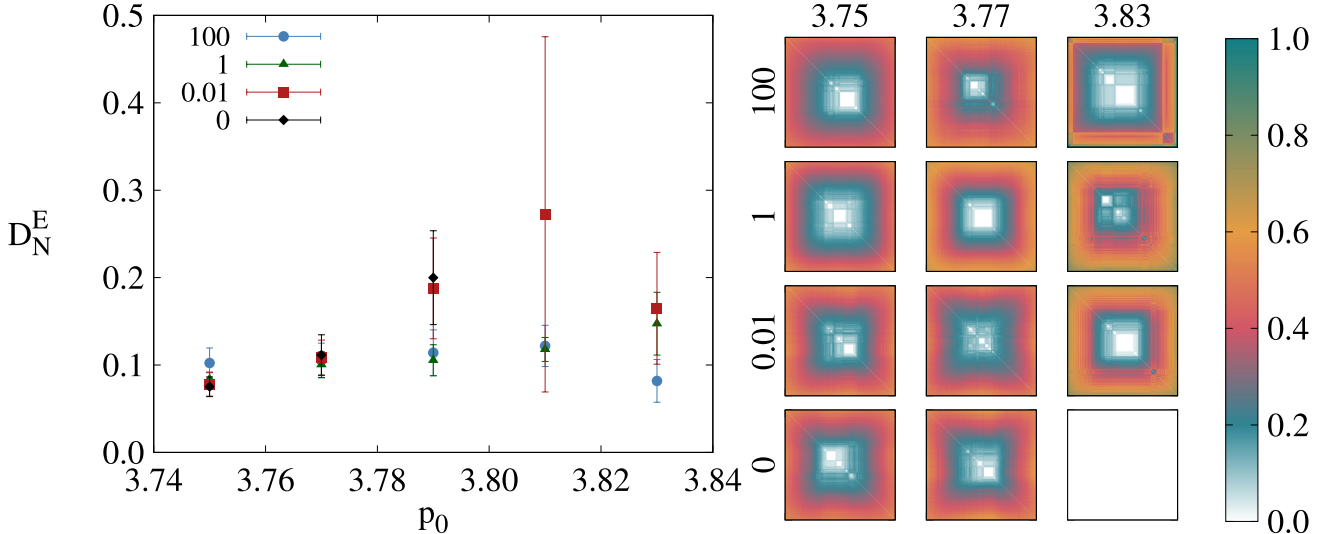


FIG. S2. (Left) Generalized distance to ultrametricity, for the normalized energy metric,  $D_N^E$ , as a function of  $p_0$ . Here we make a comparison between different  $k_A$ , using system with size  $N = 1024$ . All results are averages of 10 initial configurations subject to 100 perturbations and minimizations each. (Right) Schematic representations of the normalized energy metrics,  $d_N^E(a, b)$ , of systems with size  $N = 4096$ ,  $k_A = 0, 0.01, 1, 100$  and  $p_0 = 3.75, 3.77, 3.83$ . For  $k_A = 0$  and  $p_0 = 3.83$  the metrics only show one color since  $E_i - E_f \approx 0$  and thus the normalized metric distance diverges.

perturbations do not lead to different results and thus the range of distances found will only depend on the norm of the perturbation vector.

### E. Estimation of the rigid to fluid transition point

To estimate the transition point from a rigid to a fluid tissue we use a technique based on recent work on the vertex model [17]. We use the minimized configurations

calculated in the main text and calculate the probability of finding a configuration with zero energy,  $P[E = 0]$ , for different  $p_0$  and  $N$ . Since we have less data for the different  $p_0$  than in Ref. [17], we fit our data to a hyperbolic tangent:

$$P[E = 0](p_0) = 0.5 \left[ 1 - \tanh \left( -\frac{p_0 - a}{2b} \right) \right], \quad (\text{S1})$$

where  $a$  and  $b$  are fitting parameters. Even though we

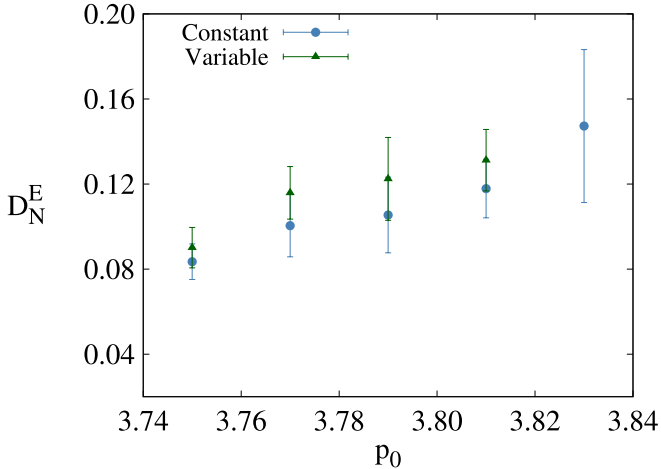


FIG. S3. Generalized distance to ultrametricity, for the normalized energy metric,  $D_N^E$ , as a function of  $p_0$ , for  $N = 1024$ . All results are averages of 10 initial configurations subject to 100 perturbations and minimizations each. The results represent the values measured using the constant  $\varepsilon_{max}$  as in the main text, and a variable one that depends on  $p_0$ .

do not expect that the actual function is Eq. (S1), it is a good approximation for the  $N$  explored here. By using this function we are able to differentiate it and calculate the probability distribution of the transition points,  $P(p_0^*) = d_{p_0} P[E = 0](p_0^*)$ , from which we can extract the peak value corresponding to the probable transition point  $p_0^*$  for a given  $N$ . Figure S5 shows how  $P[E = 0](p_0)$  increases with  $p_0$  and the corresponding fit given by Eq. (S1), which are in good agreement. The right plot shows the derivative of Eq. (S1) as a function of  $p_0^*$ . We use the value corresponding to the peak of

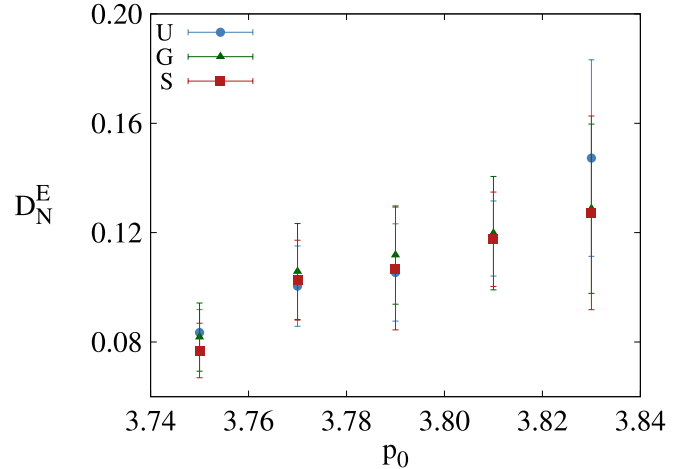


FIG. S4. Generalized distance to ultrametricity,  $D_N^E$ , as a function of  $p_0$  for the different perturbations, using the normalized energy metric,  $d_N^E(a, b)$ . U represents the perturbation used in the main text. The size of the system is  $N = 1024$  and  $\varepsilon_{max} = 0.1\sqrt{N}$  for all. The individual parameters of the perturbations are summarized in the text.

the distribution to estimate the transition points for the different  $N$ .

To estimate the transition point in the thermodynamic limit we find the best linear fit in a log-log plot, of the distance of the estimated  $p_0^*$  for each  $N$  (given by Fig. S5) to the thermodynamic transition point  $p_0^*(\infty)$ , as a function of  $1/N$ . Figure S6 shows the different curves for multiple  $p_0^*(\infty)$  where we estimate the actual value for the best linear fit. We focus only on  $N > 1024$  and estimate  $p_0^*(\infty) = 3.8022 \pm 0.0001$ . Although more simulations and a more appropriate estimation protocol could be used to quantify this value, our simple estimation is close to the one reported in previous work [27].

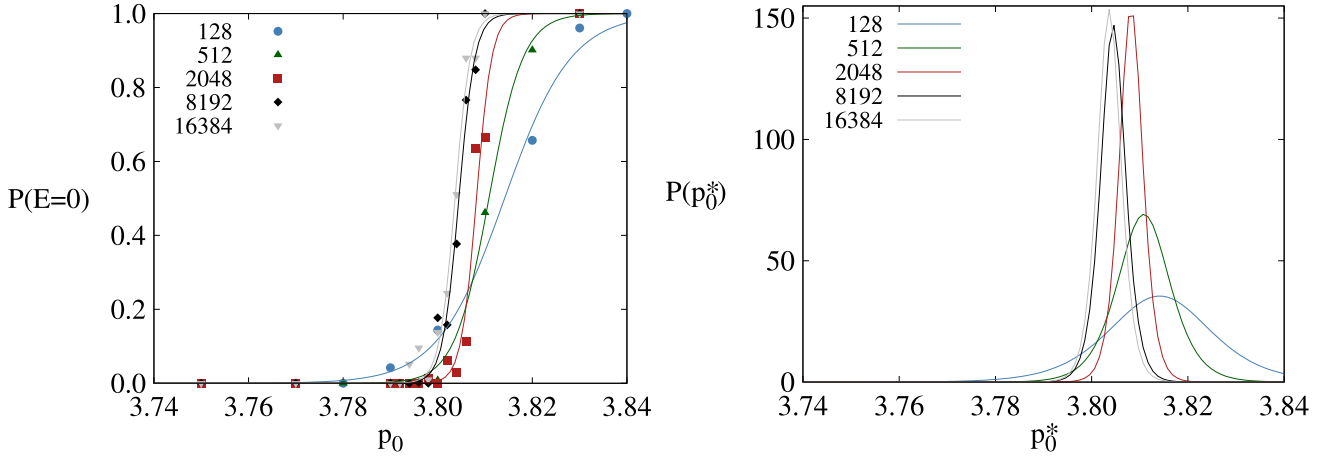


FIG. S5. On the left is plotted the probability of finding a configuration with zero energy,  $P[E = 0]$ , as a function of  $p_0$  for different  $N$ . These results were averaged over 1000 samples. We also show a fit of Eq. (S1) to the data. On the right is the estimation of the transition point,  $p_0^*$ , which is calculated using the peak value of the probability distribution function of the transition points,  $P(p_0^*) = d_{p_0^*} P[E = 0](p_0^*)$ .

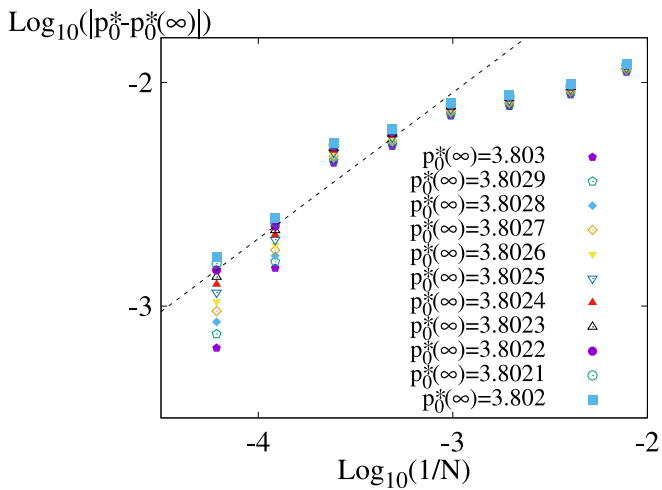


FIG. S6. Log-log plot of the absolute distance of the estimated transition points for different  $N$ s (from Fig. S5) to the thermodynamic value,  $p_0^{*(\infty)}$ , as a function of  $1/N$ . We find  $p_0^{*(\infty)} = 3.8022 \pm 0.0001$  as the value which gives the best linear fit for  $N > 1024$  and take as the estimation of the transition point.